Pressure-Induced Insulator-Metal Transition in Silicon Telluride from First-Principles Calculations

Romakanta Bhattarai and Xiao Shen*

Department of Physics and Materials Science, University of Memphis, Memphis, TN, 38152

ABSTRACT

Silicon telluride (Si₂Te₃) is a two-dimensional semiconductor with unique structural properties due to the size contrast between Si and Te atoms. A recent experiment shows that the material turns metallic under hydrostatic pressure, while the lattice structure of the metallic phase remains to be identified. In this paper, we propose two metallic phases, M1 and M2, of Si₂Te₃ using the evolution algorithm and first-principles density functional theory (DFT) calculations. Unlike the presence of Si-Si dimers in the semiconducting (SC) phase, both M1 and M2 phases have individual Si atoms, which play important roles in the metallicity. Analysis of structural properties, electronic properties, dynamical as well as thermal stability is performed. The energies of these new structures are compared with the SC phase under the subsequent hydrostatic pressure up to 12 GPa. The results show that M1 and M2 phases have lower energies under high pressure, thus elucidating the appearance of the metallic phase of Si₂Te₃. In addition, the external pressure causes the SC phase to have an indirect-direct-indirect bandgap transition. Analysis of Raman spectra of the SC phase at a different pressure shows the shifting of the major Raman peaks, and finally disappearing confirms the phase transition. The results are in good agreement with the experimental observations. The understanding of the insulator-metal phase transition increases the potential usefulness of the material system.

I. INTRODUCTION

Silicon telluride (Si₂Te₃) is a two-dimensional material with a complex structural configuration. This material has been successfully fabricated into a few atomic layers thickness in the past several years.^{1–4} Compared to other compounds such as Bi₂Te₃ and In₂Te₃, the cation size in Si₂Te₃ is small, which offers a unique opportunity to gain a broader understanding of the Me₂Te₃ family. Due to their small sizes, Si atoms form dimers and fill only 2/3 of the allowed 'metal' sites between the hexagonal close-packed Te layers,

thereby leaving the 1/3 sites vacant. The dimer orientation is possible along both in-plane and out-of-plane directions, and rotation of the dimer has an activation energy of 1 eV, indicating that it can happen at room temperature.⁵ The presence of Si-Si dimers and their possible orientations adds extra interest to the material as the dimer orientations alter the fundamental properties of the material and impact potential applications.

Si₂Te₃ is one of the rare natural p-type 2D semiconductors³ and also possesses a set of interesting properties. Theoretical investigation shows that Si₂Te₃ is one of the most flexible 2D materials.⁶ First-principles calculations and experiments show that it possesses anisotropic optical properties.^{7,8} Experiments by Wang et al. show its optoelectronic properties can be modified through doping and intercalation of Ge and Cu without altering the fundamental host lattice.⁹ Other members of the Si-Te family, such as SiTe and SiTe₂, are also confirmed and have shown interesting properties.^{10–19} A recent theoretical investigation discovered a novel structure of SiTe₂²⁰ that is more stable than the CdI₂ type that is common in MX₂ compounds, which again manifests the uniqueness of this material system.

A recent experiment by Johnson et. al²¹ shows that Si₂Te₃ nanoplates undergo a color change from red to black around a hydrostatic pressure of 9.5 GPa, indicating a phase transition to a metallic phase. Such phase transition can be observed at a relatively lower pressure around 7 GPa if Mn is intercalated between the layers. Also, the major Raman active mode in the SC phase at 144 cm⁻¹ shifts under external pressure and finally disappears, which could be the sign of phase transition. The crystal structure of the metallic Si₂Te₃ remains to be explored. In another recent experiment, Wu et al. discovered that Si₂Te₃ nanowires could be switched between the semiconducting and metallic states under external electric voltage.²² In addition, phase transition around 673-723 K was reported by Bailey,²³ Ziegler,²⁴ and Gregoriades,² which is associated with silicon dimers break up. These pressure-, electrical-, and temperature-induced phase changes make it particularly interesting to investigate other possible phases of Si₂Te₃, especially the metallic ones.

In this paper, we report a computational study of Si₂Te₃ under high pressure using the evolutionary algorithm combined with first-principles density functional theory (DFT) calculations. We propose two candidate metallic phases of Si₂Te₃ to account for the experimental observation at high-pressure. The total energies of the metallic phases are compared with the original semiconducting phase under different external pressure, from which the transition pressures are obtained and are in good agreement with experiments. We also find that the semiconducting Si₂Te₃ undergoes a bandgap transition from indirect to direct and back to indirect with the pressure. Analysis of Raman spectra shows the positive shifting of the major peak at 144 cm⁻¹ with the pressure and finally disappearing, which agrees with the experiments.

II. METHODS

We use the universal crystal structure predictor USPEX^{25,26} to investigate possible stable phases of Si₂Te₃. The predictor works under the evolutionary algorithm coupled with the first-principles density functional theory method. Identification of the global free-energy minimum is required to predict the most stable phase among all possible structures generated. A total of 30 structures are considered as the initial population, which are generated randomly by using the space group symmetry. The population in each generation is kept fixed throughout the search with the evolutionary algorithm. The stopping criterion for the evolutionary algorithm search is that the most-fit structure does not change for 15 generations. We choose 60% of the current generation to produce the next generation. In total, 50% of the population is produced by heredity, 20% produced randomly using the space group symmetry, 10% produced by soft mutation, 10% produced by lattice mutation, and the remaining 10% produced by permutation in each generation afterward. The search is carried out under an external hydrostatic pressure of 10 GPa. During the evolutionary algorithm search, first-principles DFT calculations using VASP (Vienna Ab initio Simulation Package)²⁷ package with the Perdew-Burke-Ernzerhof (PBE) exchange-correlation funcational²⁸ and the projected augmented wave method²⁹ are used to relax the structures and obtain the total energies. The maximum kinetic energy cutoff is 320 eV. The convergence criteria for electronic and ionic relaxation are respectively 10⁻⁵ eV and 10⁻⁴ eV, along with.

For accurate comparisons of the energies, the low energy structures obtained by the evolutionary algorithm are optimized further with the VASP with tighter numerical settings. Plane-wave basis set with a kinetic energy cutoff of 500 eV is used for the expansion of wavefunction. The criteria for electronic and force convergence are set to 10^{-9} eV and 10^{-4} eV/Å, respectively. Gamma centered k-point grids of $9\times9\times5$, $9\times9\times9$, and $13\times13\times5$ are used in the integration of Brillouin zones for the semiconducting (SC) phase and two metallic phases, respectively. The calculations use both PBE²⁸ and PBEsol³⁰ versions of the exchange-correlation functional. The dynamical stability of both metallic structures is confirmed by the phonon spectra obtain using Phonopy package,³¹ which uses the finite displacement method with supercells. The dynamical stability is further verified by the ab initio molecular dynamics simulations using the supercells containing 160 atoms and 90 atoms for M1 and M2 phases at 500 K for 30 ps with a time step of 2 fs.

The Raman spectra of the SC phase under different pressures are calculated using the density functional perturbation theory (DFPT).³² We use the Quantum Espresso package³³ with the norm-conserving pseudopotential generated via Rappe-Rabe-Kaxiras-Joannopoulos method.³⁴ The exchange-correlation functional of PBE type is used in the calculations. Plane-wave basis sets with the cutoff energy of 80 Rydberg (Ry) is used for the expansion of wave function. The energy and force are converged to 10⁻⁸ Ry and 10⁻⁷ Ry/Bohr, respectively, during the geometrical optimization. Brillouin zone is sampled with a 9×9×5 k-points grid centered at Gamma point. The total energy is converged to 10⁻¹² Ry and 10⁻¹⁴ Ry in self-consistent and

phonon calculations, respectively. Finally, Raman coefficients are computed from the second-order response function.³⁵

III. RESULTS & DISCUSSION

The global search for the low energy configurations of Si₂Te₃ using the evolutionary algorithm with USPEX and the density functional theory is done for the unit cells consisting of 5 to 80 atoms. During the search, an external pressure of 10 GPa is applied to explore the stable high-pressure phases of Si₂Te₃. A total of 2398 structures are generated, among which we find two structures with the lowest energy: one with ten atoms per unit cell and another with five atoms per unit cell, which are named as M1 and M2 phases. We compare the energy per atom on both the phases under PBE and PBEsol functionals. Under PBE functional, energy per atom of M1 and M2 are -3.91 eV & -3.90 eV at 10 GPa respectively. However, under PBEsol, the respective values are -3.30 eV & -3.32 eV at 10 GPa. The very small energy difference is within the error bars associated with the exchange-correlation functional. Thus, we can only conclude that they are close in energy and could both exist in nature.

The crystal structures of the M1 and M2 phases are shown in Figure 1 and Figure 2, respectively. Both M1 and M2 phases maintain the stoichiometry of Si₂Te₃. The corresponding lattice parameters of M1 and M2 are shown in Table I. The M1 phase has a hexagonal crystal lattice, whereas the M2 has a triclinic crystal lattice. (The predicted X-ray diffraction spectra of the M1 and M2 phases are in the Supporting Information.) We also explored ABAB and ABCABC types of stacking of the layers in the M1 phase. It is found that the energies of different stacking only differ by less than 1 meV. Therefore, different stackings are likely to occur in bulk and multiplayer of the M1 phase. In this work, we focus on the configuration shown in Fig. 1. To the best of our knowledge, these two structures have not been reported in other 2D chalcogenides.

The disappearance of the van der Waals gaps under high-pressure has been reported in a number of 2D materials, such as VSe₂,³⁶ TiTe₂,³⁷ BiTeBr,³⁸ SnSb₂Te₄,³⁹ LaO_{0.5}F_{0.5}BiS₂,⁴⁰ and InSe.⁴¹ The M1 and M2 phases of Si₂Te₃, on the other hand, are layered. In this regard, Si₂Te₃ are similar to black phosphorus,^{42,43} MoS₂,^{44,45} FePS₃,⁴⁶ FePSe₃,⁴⁷ MoSe₂,⁴⁸ MoTe₂,⁴⁹ MoSSe,⁵⁰ Bi₂Te₃,⁵¹ and PbFCl⁵², which remains layered at pressures greater than 4-5 GPa.

Table I: Structural parameters of the predicted M1 and M2 phases of Si₂Te₃

Phase	a (Å)	b (Å)	c (Å)	α (°)	β (°)	γ (°)	Bravais lattice
-------	-------	-------	-------	-------	-------	-------	-----------------

M1	6.82	6.82	7.48	90	90	60	Hexagonal
M2	3.90	3.90	10.93	100.26	90.07	120	Triclinic
SC (Ref. 5)	7.54	7.94	14.15	90.00	90.00	120.00	Trigonal

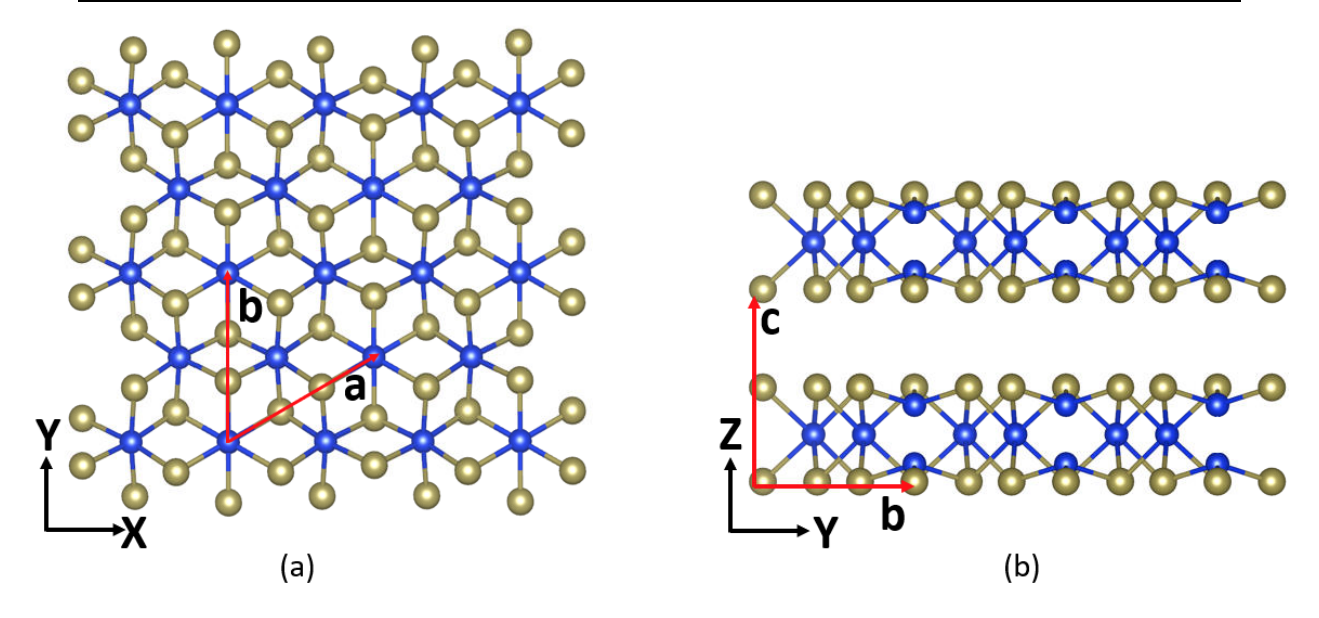


Figure 1: (a) Top and (b) side views of M1 phase of Si₂Te₃ with lattice vectors marked by solid red lines. Te and Si atoms are represented in tan and blue color, respectively.

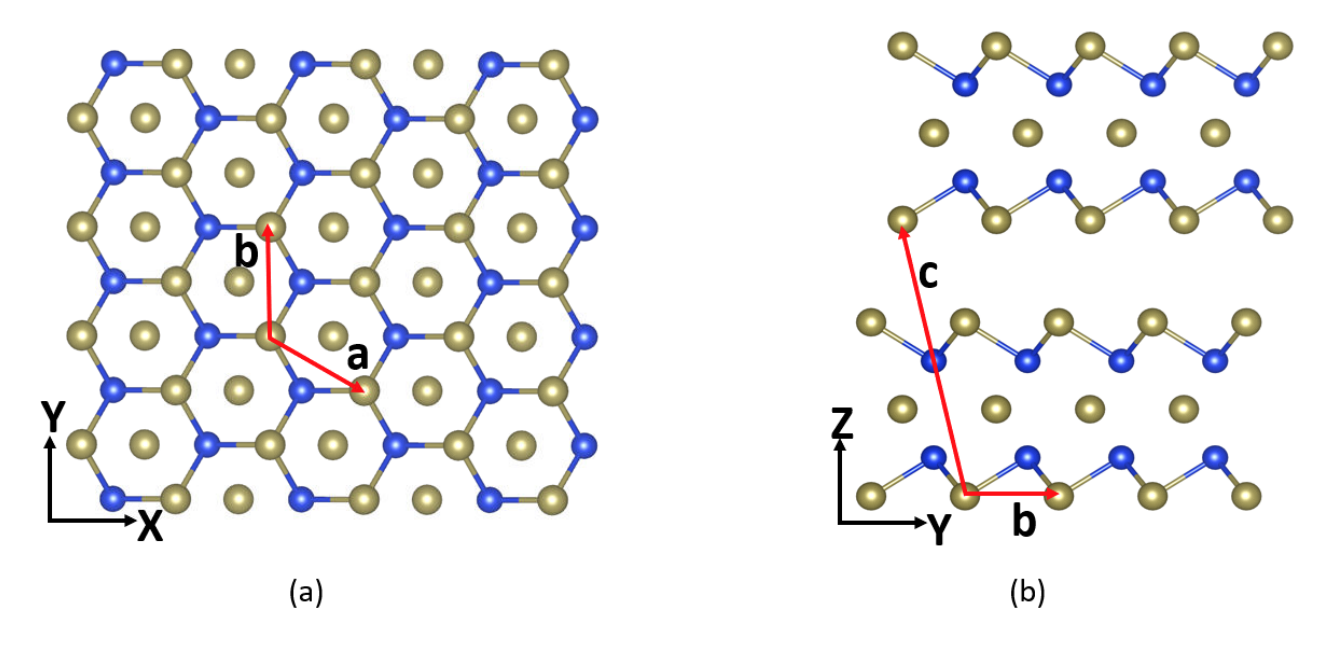


Figure 2: (a) Top and (b) side views of the M2 phase of Si₂Te₃.

The dynamical stabilities of M1 and M2 are tested under phonon dispersion calculation using the finite displacement method with supercells of 160 atoms at 10 GPa pressure. The phonon spectra have no imaginary phonon modes, as shown in Figure 3(a) and 4(a), confirming their dynamical stabilities. We further confirm their dynamical stability by performing the ab-initio molecular dynamic (AIMD) simulation of both phases at 500 K and 10 GPa, which are shown in Figures 3(b) and 4(b) for the M1 and M2 phases, respectively. No structure reconstruction is found over the entire 30 ps. The fluctuation of the total energy per atom during the simulation time of 30 ps without any sudden drop confirms that both the phases are dynamically stable at 10 GPa pressure.

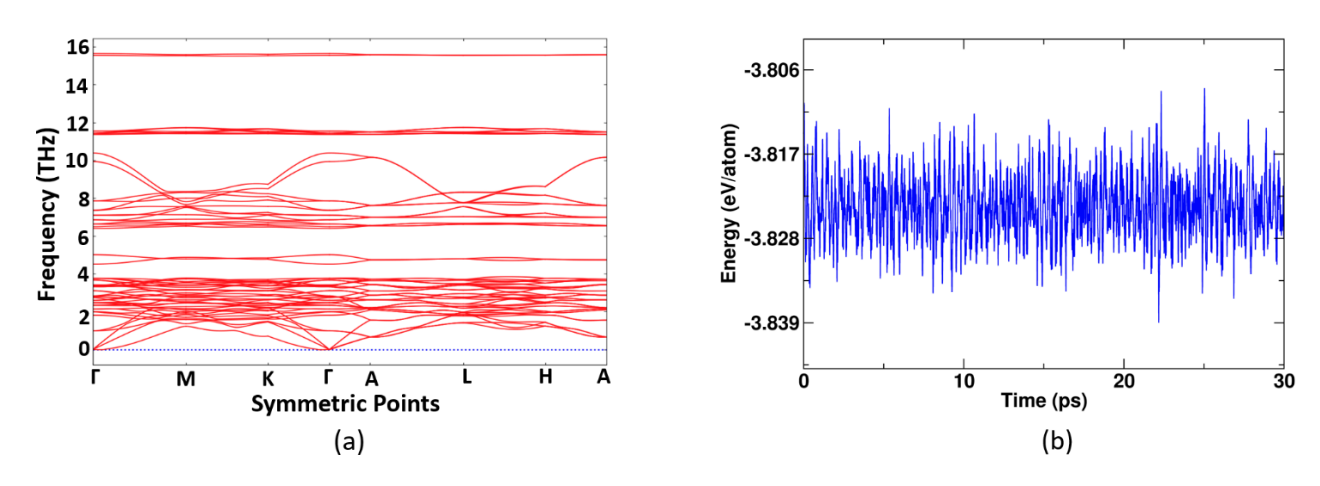


Figure 3. (a) Phonon band structures of the M1 phase. (b) Energy of the M1 phase during AIMD simulation at 500 K over 30 ps.

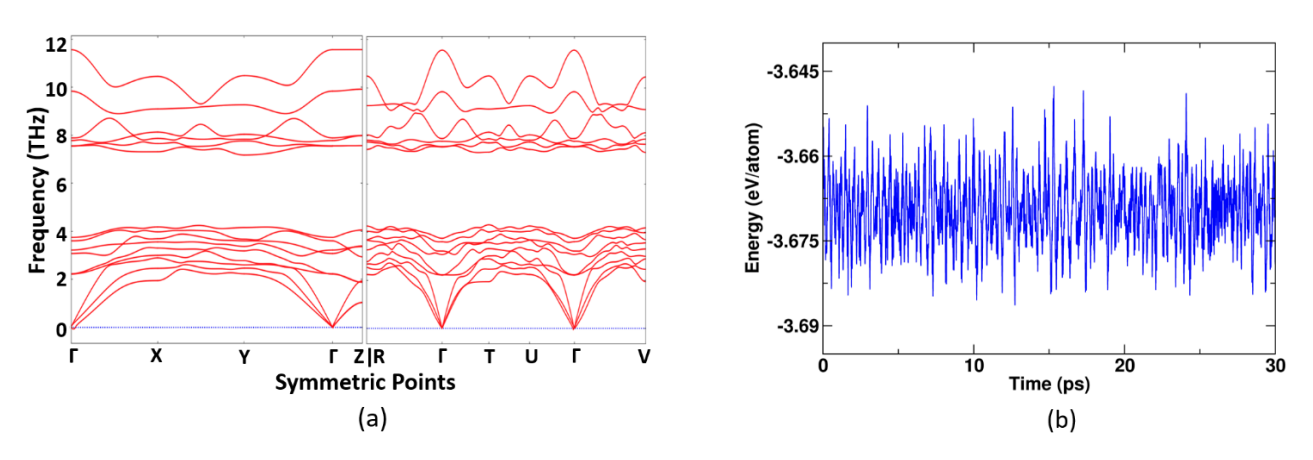


Figure 4. (a) Phonon band structures of the M2 phase. (b) Energy of the M2 phase during AIMD simulation at 500 K over 30 ps.

Next, we discuss the electronic properties of the M1 and M2 phases. Figure 5 shows the electronic band structures and densities of states (DOS) obtained using DFT with the spin-orbit interaction. From the band structure of the M1 phase (Figure 5(a)), we can see there is no bandgap, indicating the phase is metallic. The corresponding partial and total DOS of M1 is plotted in Figure 5(b). It shows that the p-orbital of the Te atom mainly constitutes the valence band, whereas the p-orbital of both the Si and Te atom have major contributions to the conduction band. There is a small contribution also coming from the s-orbital of Si and Te atoms as well as the d-orbital of Te atom. Similar patterns are seen in Figures 5(c) and 5(d) for the M2 phase, where both the band structures and DOS indicate the metallic nature. As the DFT method is known to underestimate the band gap, to further verify the metallic nature of the M1 and M2 phases, we perform hybrid DFT (HSE06^{53,54}) calculation. Both the band structures and DOS from the HSE method (see Supporting Information) confirm that M1 and M2 are metallic.

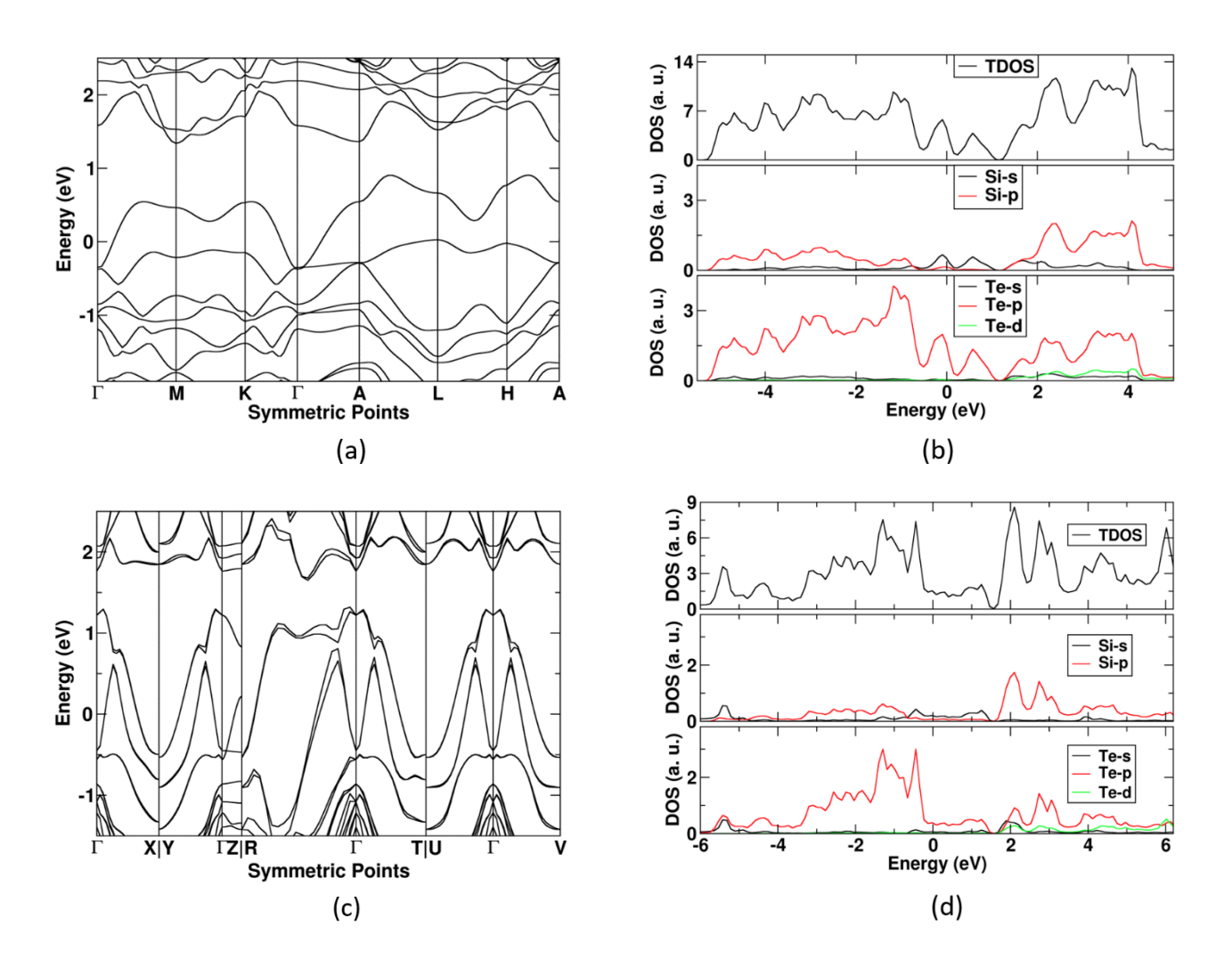


Figure 5: (a) Electronic band structures of the M1 phase along the high symmetric points in Brillouin zone. (b) Partial and total DOS of the M1 phase. (c) Electronic band structures of the M2 phase along the high symmetric points in Brillouin zone. (d) Partial and total DOS of the M2 phase. Effect of spin orbit coupling is considered in the calculations.

To get a deeper insight into the electronic properties of Si₂Te₃, we perform the Bader charge analysis on the M1 and M2 phases and compare them with the result from the well-known SC phase. In the M1 phase, we found that the amount of charge transferred from each Si atom is not the same. A charge of 0.523e is transferred from half of the Si atoms (labeled as Si1 in Figure 6(a)), whereas 0.459e is transferred from other halves (labeled as Si2 in Figure 6(a)). However, the amount of charge received by each Te atom is the same, which is 0.327e. This kind of transfer mechanism is found to be opposite in the M2 phase, where a total of 0.483e charge gets transferred from each Si atom, but the amount of charge gained by all Te atoms is not the same throughout the cell. Each Te atom at the surface gets 0.339e charge, whereas a Te atom in the middle layer gets relatively less charge (0.288e) as compared to the surface atom. The higher charge in Te atoms at the surface is higher than in the middle layer, making the surface more conducting. In the semiconducting phase, each Si atom transfers a 0.609e charge, whereas each Te atom gets a 0.406e amount of charge.

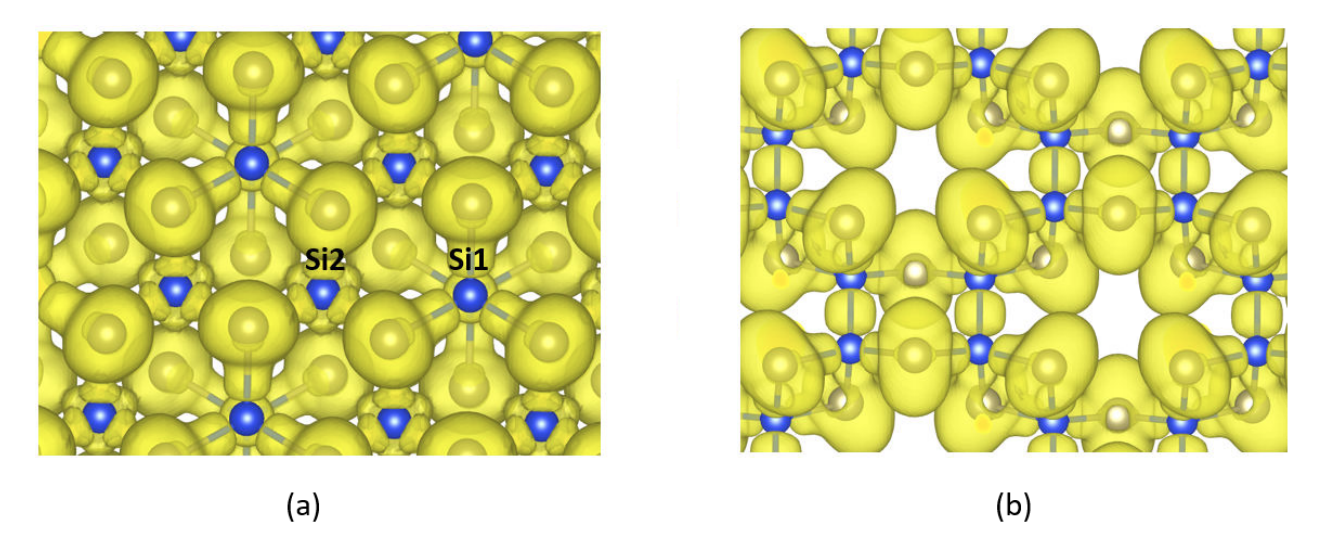


Figure 6. Top views of the electron localization function (ELF) in the M1 (a) and SC (b) phases of Si₂Te₃. The iso-surface level is 0.72 in each case.

To explain the charge transfer mechanism in various phases, we analyze the chemical bonding in Si_2Te_3 using the electron localization function (ELF). Figures 6(a) and 6(b) are top views of the M1 and SC

phases, respectively. In Fig. 6(a), we observe two different types of bonding in the M1 phase: every Te atom has a lone pair and participates in one Si-Te bond that indicates covalent bonding. However, only half of the Si atoms (marked as Si1 in Fig. 6(a)) participates in the Si-Te bonds. The remaining half of the Si atoms (marked as Si2) are not bonded to Te. This is consistent with the different amounts of charge transferred pates from two types of Si atoms, as discussed above. Meanwhile, in the SC phase, each Si atom participates in one Si-Si bond and three Si-Te bonds, and each Te atom participates in two Si-Te bonds and possesses one lone pair, as shown in Figure 6(b). This result matches with the discussion above that all Si atoms in the SC phase are losing charge equally, and all Te atoms are gaining charge equally.

Next, we analyze the ELF in the M2 phase and compare it with that in the SiTe structure. The reason for such comparison is that the top and bottom surfaces of the M2 phase of Si₂Te₃ is similar to SiTe. Figure 7(a) and 7(b) are the side views of the M2 phase and SiTe, respectively. In Figure 7(a), it is clearly seen the upper and lower Te atoms (i.e., surface atoms) feature lone pair and Si-Te bond. Meanwhile, there is no indication of Si-Te bonds in the middle Te layer. The ELF profiles of the top and bottom layers are very similar to that of the bulk SiTe structure, which is shown in Figure 7(b). This similarity led us to conclude that the Si atoms are covalently bonded with the surface Te atoms. Meanwhile, as the Te atoms in the middle are slightly negatively charged, they likely form ionic bonding with the positive Si atoms. Such a layer of Te atoms may have interesting electronic transport properties (see Supporting Information for the charge density at the Fermi level).

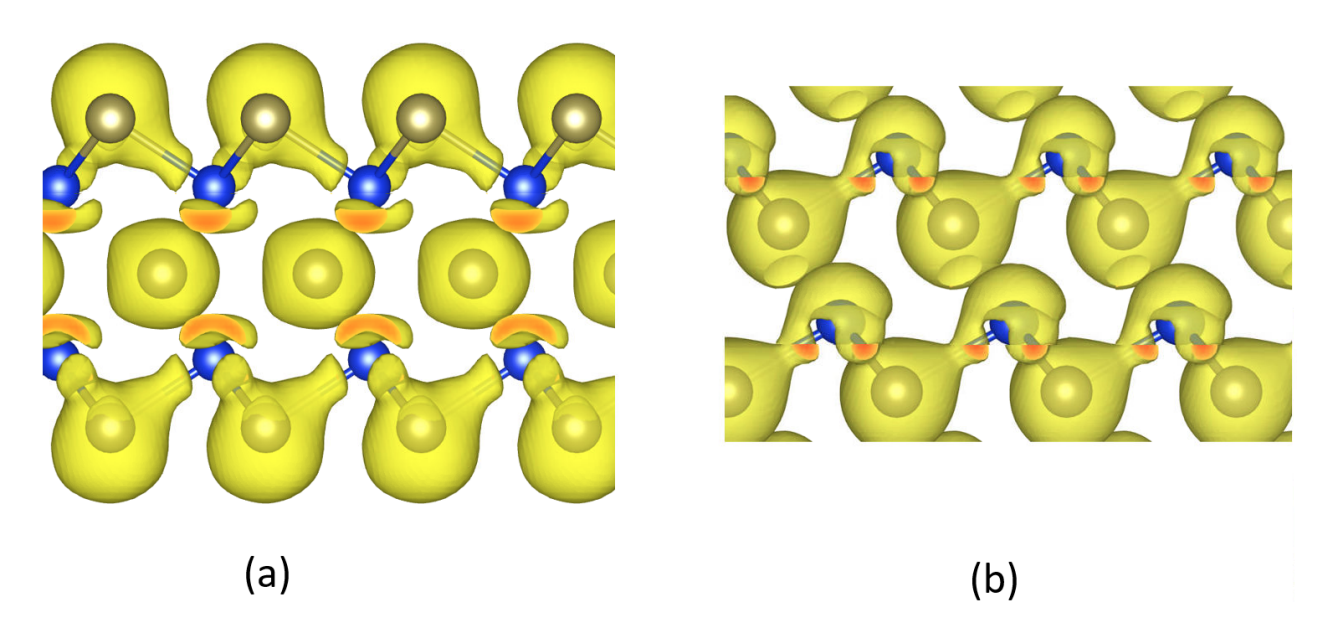


Figure 7. Side views of ELF in the M2 phase of Si₂Te₃ (a) and SiTe (b). The iso-surface level is 0.73 in each case.

We now discuss the effect of external hydrostatic pressure on the SC phase of Si₂Te₃. First, we calculate the phase transition pressure. We take all three phases viz; the M1, M2, and SC phases of Si₂Te₃ and apply a subsequent hydrostatic pressure up to 12 GPa. The energies per atom of each phase in the pressure range of 0-12 GPa are shown in Figure 8(a). Initially, when the pressure is not applied, the total energy per atom of M1, M2, and SC phases are -4.04, -4.01, and -4.12 eV, respectively. As the SC phase is the lowest in total energy, it is the ground state at low pressures. However, upon applying the pressure, the energy of the SC phase is found to increases faster as compared to M1 and M2 and exceeds the M1 phase beyond 7.4 GPa and M2 phase beyond 8.7 GPa. It implies that at 7.4 GPa, there is a phase transition from semiconductor to metal and the resulting metallic phase (M1) has the lower energy. Also, at 8.7 GPa, there could be another phase transition from the SC phase to the metallic M2 phase. The transition pressures of 7.4 GPa and 8.7 GPa are in agreement with the experimental value of 9.5 GPa.²¹ It could also be possible that the phase observed experimentally was actually either the M1 or the M2 phase or a mixture of the two. Future experiments may resolve this. This possibility of two stable phases of Si₂Te₃ adds extra interest to the Si-Te compounds.

We also find that the SC phase undergoes an unusual indirect-direct-indirect band gap transition with the increase of hydrostatic pressure. Figure 8(b) shows the band gap of the SC Si₂Te₃ as a function of applied pressure from DFT calculations using the PBE functional, including the spin-orbital interaction. It can be seen that the band gap decreases from 1.48 eV to 0.31 eV as the pressure changes from 0 to 10 GPa. We observe two kinks in the curve that indicate changes in the nature of the band gap. The gap at 0 GPa is 1.48 eV and is indirect. However, the application of hydrostatic pressure changes the band gap to direct at 1.2 GPa. The band gap remains direct up to 6.7 GPa, beyond which (the next data point is calculated at 6.8 GPa) it changes back to indirect and remains so until the material transitions to the metallic phase. It is interesting to note that a similar pattern of band gap variation and direct-indirect transition with uniaxial strain was also observed in the monolayer Si₂Te₃.⁶

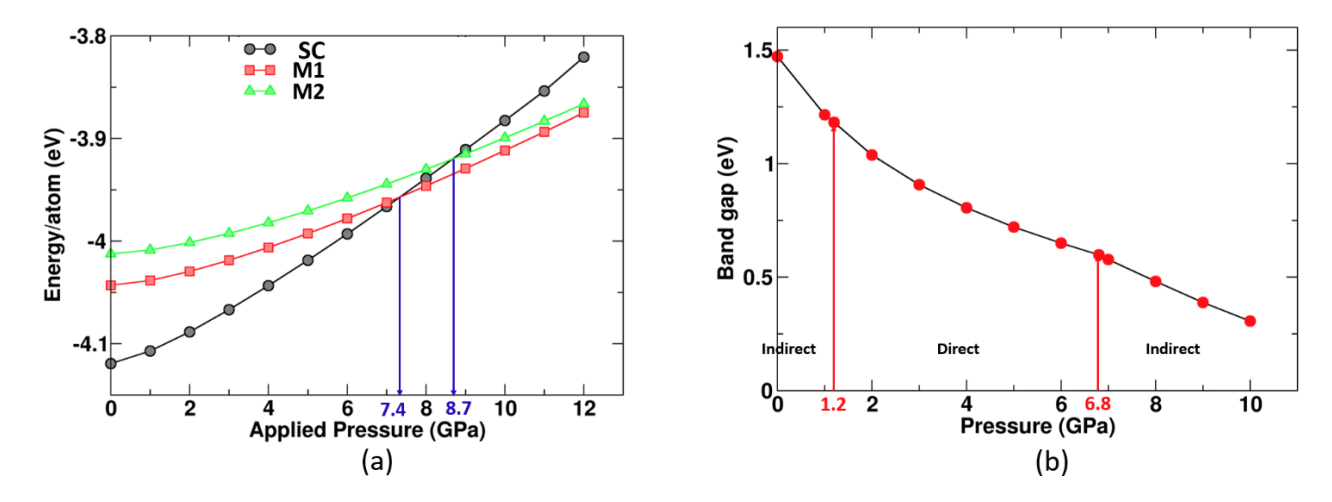


Figure 8: (a) Variation of energy per atom of the SC, M1 and M2 phases of Si₂Te₃. (b) DFT-PBE band gap as a function of the applied hydrostatic pressure in the SC phase showing indirect-direct-indirect band gap transitions.

A detailed analysis of the band gap transition is shown in the band structures in Figure 9. At 0 GPa, the VBM of the SC Si₂Te₃ lies at the X point in the Brillouin zone, whereas the CBM lies at the Gamma point, resulting in an indirect band gap (Fig 9(a)). As the pressure increases, the CBM shifts towards the X points and arrives at it at 1.2 GPa, thus changing the band gap to direct. The positions of CBM and VBM remain at X points (Fig. 9(b)) up to 6.7 GPa, but as the pressure increase further, the VBM starts to shift towards the Gamma points, causing the band gap to be indirect again (Fig. 9(c)). These shifts in CBM and VBM locations indicate that both the electrons and holes in the SC Si₂Te₃ are strongly influenced by the pressure.

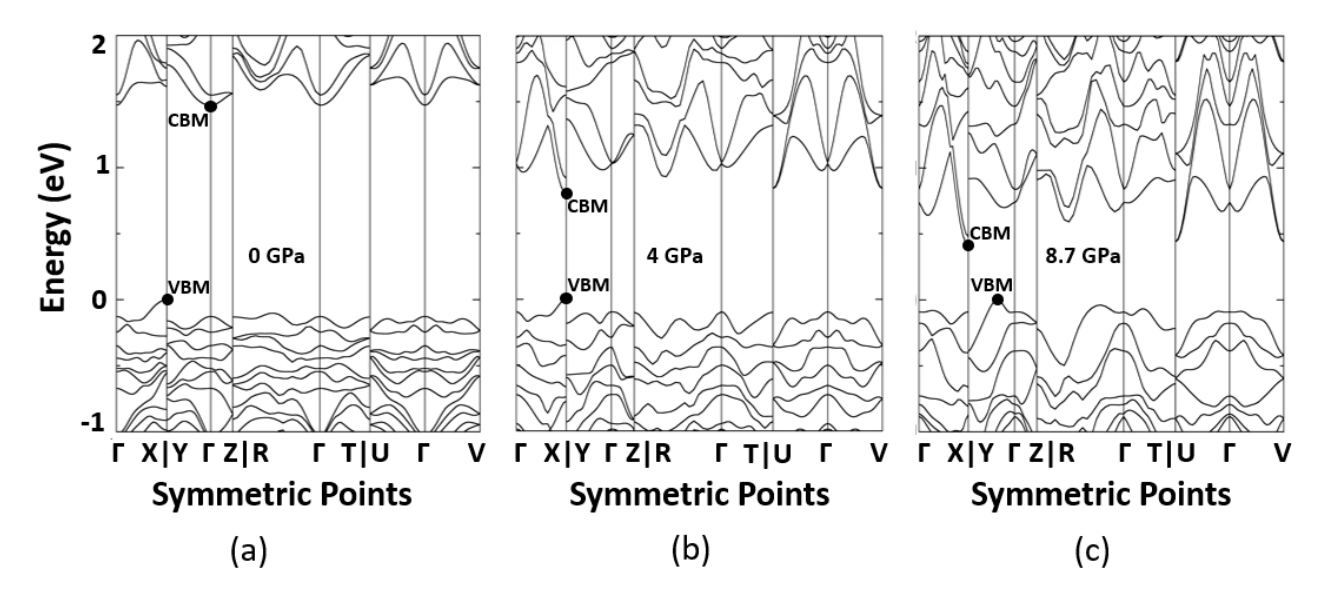


Figure 9: Electronic band structures of the SC phase of Si₂Te₃ under DFT with the PBE functional at different pressures showing the gap transition. VBM and CBM refer to the valence band maximum and conduction band minimum. Spin-orbit interaction is considered in the calculation.

In the SC phase of Si₂Te₃ under ambient pressure, there is a very strong Raman peak at 144 cm⁻¹, which is a well-known A_{1g} mode, along with several other active peaks. Johnson et al. observed that the major Raman peak shifts to higher frequency under external pressure and disappearance at the pressure greater than 10 GPa.²¹ To compare with the experiment, we calculate the Raman spectra of the SC phase of Si₂Te₃ under different pressures up to 12 GPa. The results are shown in Figure 10. The calculated Raman spectrum at 0 GPa has been previously published as Fig. 6 in Ref. 8 and shows good agreement with the experimental Raman spectrum taken at low temperature (Fig. 4a in Ref. 8). We find a major Raman peak at 144 cm⁻¹ at 0 GPa, which agrees well with the experimental value of 144 cm⁻¹. The calculated Raman peak shifts towards higher frequencies (wavenumbers) as the pressure increases. At 10 GPa, the peak position has changed to 162 cm⁻¹, which is close to the experimental value of 167 cm⁻¹ at 9.86 GPa. Overall, the calculations of Raman peak position and the pressure-induced shift are in excellent agreement with experiments.

Next, we discuss the disappearance of Raman peak at pressures greater than 10 GPa. Ideal metals do not have Raman active phonon modes due to the screening from free charge carriers. However, the screening can be incomplete in 2D metals such as the metallic MoS₂, where Raman signals have been experimentally observed.⁵⁵ The absence of the Raman peak at high pressure in the experiment can be due to either sufficient screening in the metallic nanoplates or the changes in the phonon modes upon the phase transition. Since the M1 and M2 phases are metallic, it is not possible to directly carry out calculations of

Raman intensities using the DFPT method. Alternatively, we examine the vibrational modes of the M1 and M2 phases obtained from phonon calculations. No phonon mode is found near the position of the major Raman peak in the SC phase (144 cm⁻¹ at 0 GPa and 162 cm⁻¹ at 10 GPa). The results suggest that the absence of the A_{1g} mode near 144 cm⁻¹ can be used to identify the phase transition to the M1 and M2 phases, even in experiments with smaller and thinner samples.

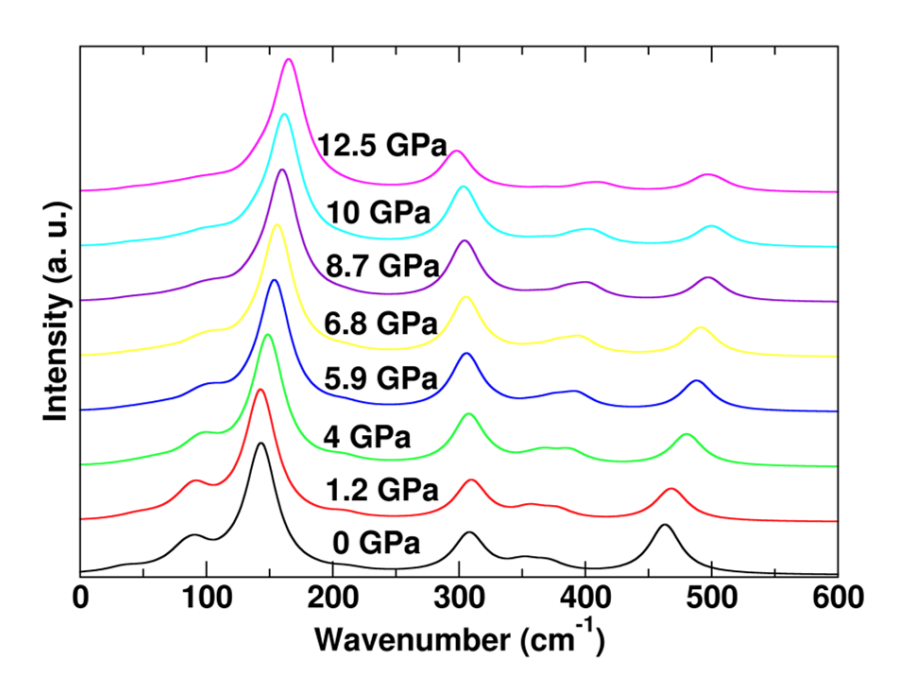


Figure 10: Calculated Raman spectra of the SC phase of Si₂Te₃ under different pressure.

IV. CONCLUSION

Two candidate structures, M1 and M2, of the high-pressure metallic phase of Si₂Te₃, are discovered using the evolution algorithm and first-principles density functional theory calculations. Analysis of structural, electronic, and vibrational properties is performed. A comparison of energies of new structures with the well-known SC phase as a function of hydrostatic pressure reveals insulator-metal phase transition pressure around 7.4 to 8.7 GPa. Also, the external pressure causes the SC phase to have an indirect-direct-indirect bandgap transition. The calculated Raman spectra of the SC phase shows the shifting of the major peaks towards higher wavenumbers with increasing pressure and finally disappearing upon the phase transition. These results are in agreement with the experimental observations. Overall, the findings highlight the rich structures and properties of Si₂Te₃ and the Si-Te system.

Supporting Information

Prediction of XRD spectra. Electronic structure from hybrid functional. Charge density at the Fermi level. Crystallographic data of the M1 and M2 phases of Si₂Te₃.

AUTHOR INFORMATION

Corresponding Author: Xiao Shen, email: xshen1@memphis.edu.

Acknowledgment:

This work was supported by the National Science Foundation grant # DMR 1709528 and by the Ralph E. Powe Jr. Faculty Enhancement Awards from Oak Ridge Associated Universities (ORAU). The computational resources were provided by the NSF XSEDE grant number TG-DMR 170064 and 170076 and the University of Memphis High-Performance Computing Center (HPCC).

References:

- (1) Ploog, K.; Stetter, W.; Nowitzki, A.; Schönherr, E. Crystal Growth and Structure Determination of Silicon Telluride Si2Te3. *Mater. Res. Bull.* **1976**, *11*, 1147–1153.
- (2) Gregoriades, P. E.; Bleris, G. L.; Stoemenos, J. Electron Diffraction Study of the Si2Te3 Structural Transformation. *Acta Crystallogr. B* **1983**, *39*, 421–426.
- (3) Keuleyan, S.; Wang, M.; Chung, F. R.; Commons, J.; Koski, K. J. A Silicon-Based Two-Dimensional Chalcogenide: Growth of Si2Te3 Nanoribbons and Nanoplates. *Nano Lett.* **2015**, *15*, 2285–2290.
- (4) Ziegler, K.; Birkholz, U. Photoelectric Properties of Si2Te3 Single Crystals. *Phys. Status Solidi A* **1977**, *39*, 467–475.
- (5) Shen, X.; Puzyrev, Y. S.; Combs, C.; Pantelides, S. T. Variability of Structural and Electronic Properties of Bulk and Monolayer Si2Te3. *Appl. Phys. Lett.* **2016**, *109*, 113104.
- (6) Bhattarai, R.; Shen, X. Ultra-High Mechanical Flexibility of 2D Silicon Telluride. *Appl. Phys. Lett.* **2020**, *116*, 023101.
- (7) Bhattarai, R.; Chen, J.; Hoang, T. B.; Cui, J.; Shen, X. Anisotropic Optical Properties of 2D Silicon Telluride. *MRS Adv.* **2020**, 1–9.
- (8) Chen, J.; Bhattarai, R.; Cui, J.; Shen, X.; Hoang, T. Anisotropic Optical Properties of Single Si2Te3 Nanoplates. *Sci. Rep.* **2020**, *10*, 19205.
- (9) Wang, M.; Lahti, G.; Williams, D.; Koski, K. J. Chemically Tunable Full Spectrum Optical Properties of 2D Silicon Telluride Nanoplates. *ACS Nano* **2018**, *12*, 6163–6169.

- (10) Weiss, A.; Weiss, A. Siliciumchalkogenide. IV. Zur Kenntnis von Siliciumditellurid. *Z. Für Anorg. Allg. Chem.* **1953**, *273*, 124–128.
- (11) Rau, J. W.; Kannewurf, C. R. Intrinsic Absorption and Photoconductivity in Single Crystal SiTe2. *J. Phys. Chem. Solids* **1966**, *27*, 1097–1101.
- (12) Lambros, A. P.; Economou, N. A. The Optical Properties of Silicon Ditelluride. *Phys. Status Solidi B* **1973**, *57*, 793–799.
- (13) Taketoshi, K.; Andoh, F. Structural Studies on Silicon Ditelluride (SiTe2). *Jpn. J. Appl. Phys.* **1995**, *34*, 3192.
- (14) Prajapat, C. L.; Gonal, M. R.; Mishra, P. K.; Mishra, R.; Sastry, P. U.; Ravikumar, G. Transport and Magnetic Properties of SiTe2. *AIP Conf. Proc.* **2017**, *1832*, 130011.
- (15) Kandemir, A.; Iyikanat, F.; Sahin, H. Stability, Electronic and Phononic Properties of β and 1T Structures of SiTex (x= 1, 2) and Their Vertical Heterostructures. *J. Phys. Condens. Matter* **2017**, *29*, 395504.
- (16) Wang, Y.; Gao, Z.; Zhou, J. Ultralow Lattice Thermal Conductivity and Electronic Properties of Monolayer 1T Phase Semimetal SiTe2 and SnTe2. *Phys. E Low-Dimens. Syst. Nanostructures* **2019**, *108*, 53–59.
- (17) Mishra, R.; Mishra, P. K.; Phapale, S.; Babu, P. D.; Sastry, P. U.; Ravikumar, G.; Yadav, A. K. Evidences of the Existence of SiTe2 Crystalline Phase and a Proposed New Si–Te Phase Diagram. *J. Solid State Chem.* **2016**, *237*, 234–241.
- (18) Göbgen, K. C.; Steinberg, S.; Dronskowski, R. Revisiting the Si–Te System: SiTe2 Finally Found by Means of Experimental and Quantum-Chemical Techniques. *Inorg. Chem.* **2017**, *56*, 11398–11405.
- (19) Chen, Y.; Sun, Q.; Jena, P. SiTe Monolayers: Si-Based Analogues of Phosphorene. *J. Mater. Chem. C* **2016**, *4*, 6353–6361.
- (20) Bhattarai, R.; Shen, X. Predicting a Novel Phase of 2D SiTe2. ACS Omega 2020, 5, 16848–16855.
- (21) Johnson, V. L.; Anilao, A.; Koski, K. J. Pressure-Dependent Phase Transition of 2D Layered Silicon Telluride (Si2Te3) and Manganese Intercalated Silicon Telluride. *Nano Res.* **2019**, *12*, 2373–2377.
- (22) Wu, K.; Chen, J.; Shen, X.; Cui, J. Resistive Switching in Si2Te3 Nanowires. *AIP Adv.* **2018**, *8*, 125008.
- (23) Bailey, L. G. Preparation and Properties of Silicon Telluride. J. Phys. Chem. Solids 1966, 27, 1593–1598.
- (24) Ziegler, K.; Junker, H.-D.; Birkholz, U. Electrical Conductivity and Seebeck Coefficient of Si2Te3 Single Crystals. *Phys. Status Solidi A* **1976**, *37*, K97–K99.
- (25) Oganov, A. R.; Lyakhov, A. O.; Valle, M. How Evolutionary Crystal Structure Prediction Works—and Why. *Acc. Chem. Res.* **2011**, *44*, 227–237.
- (26) Lyakhov, A. O.; Oganov, A. R.; Stokes, H. T.; Zhu, Q. New Developments in Evolutionary Structure Prediction Algorithm USPEX. *Comput. Phys. Commun.* **2013**, *184*, 1172–1182.
- (27) Kresse, G.; Furthmüller, J. Efficient Iterative Schemes for Ab Initio Total-Energy Calculations Using a Plane-Wave Basis Set. *Phys. Rev. B* **1996**, *54*, 11169–11186.
- (28) Perdew, J. P.; Burke, K.; Ernzerhof, M. Generalized Gradient Approximation Made Simple. *Phys. Rev. Lett.* **1996**, 77, 3865–3868.
- (29) Blöchl, P. E. Projector Augmented-Wave Method. *Phys. Rev. B* **1994**, *50*, 17953–17979.

- (30) Perdew, J. P.; Ruzsinszky, A.; Csonka, G. I.; Vydrov, O. A.; Scuseria, G. E.; Constantin, L. A.; Zhou, X.; Burke, K. Restoring the Density-Gradient Expansion for Exchange in Solids and Surfaces. *Phys. Rev. Lett.* **2008**, *100*, 136406.
- (31) Togo, A.; Tanaka, I. First Principles Phonon Calculations in Materials Science. *Scr. Mater.* **2015**, *108*, 1–5.
- (32) Gonze, X.; Vigneron, J.-P. Density-Functional Approach to Nonlinear-Response Coefficients of Solids. *Phys. Rev. B* **1989**, *39*, 13120–13128.
- (33) Giannozzi, P.; Baroni, S.; Bonini, N.; Calandra, M.; Car, R.; Cavazzoni, C.; Ceresoli, D.; Chiarotti, G. L.; Cococcioni, M.; Dabo, I.; et al. QUANTUM ESPRESSO: A Modular and Open-Source Software Project for Quantum Simulations of Materials. *J. Phys. Condens. Matter* **2009**, *21*, 395502.
- (34) Rappe, A. M.; Rabe, K. M.; Kaxiras, E.; Joannopoulos, J. D. Optimized Pseudopotentials. *Phys. Rev. B* **1990**, *41*, 1227–1230.
- (35) Lazzeri, M.; Mauri, F. First-Principles Calculation of Vibrational Raman Spectra in Large Systems: Signature of Small Rings in Crystalline S i O 2. *Phys. Rev. Lett.* **2003**, *90*, 036401.
- (36) Sereika, R.; Park, C.; Kenney-Benson, C.; Bandaru, S.; English, N. J.; Yin, Q.; Lei, H.; Chen, N.; Sun, C.-J.; Heald, S. M.; et al. Novel Superstructure-Phase Two-Dimensional Material 1T-VSe2 at High Pressure. *J. Phys. Chem. Lett.* **2020**, *11*, 380–386.
- (37) Rajaji, V.; Dutta, U.; Sreeparvathy, P. C.; Sarma, S. Ch.; Sorb, Y. A.; Joseph, B.; Sahoo, S.; Peter, S. C.; Kanchana, V.; Narayana, C. Structural, Vibrational, and Electrical Properties of 1 T TiT e 2 under Hydrostatic Pressure: Experiments and Theory. *Phys. Rev. B* **2018**, *97*, 085107.
- (38) Ohmura, A.; Higuchi, Y.; Ochiai, T.; Kanou, M.; Ishikawa, F.; Nakano, S.; Nakayama, A.; Yamada, Y.; Sasagawa, T. Pressure-Induced Topological Phase Transition in the Polar Semiconductor BiTeBr. *Phys. Rev. B* **2017**, *95*, 125203.
- (39) Sans, J. A.; Vilaplana, R.; da Silva, E. L.; Popescu, C.; Cuenca-Gotor, V. P.; Andrada-Chacón, A.; Sánchez-Benitez, J.; Gomis, O.; Pereira, A. L. J.; Rodríguez-Hernández, P.; et al. Characterization and Decomposition of the Natural van Der Waals SnSb2Te4 under Compression. *Inorg. Chem.* **2020**, *59*, 9900–9918.
- (40) Tomita, T.; Ebata, M.; Soeda, H.; Takahashi, H.; Fujihisa, H.; Gotoh, Y.; Mizuguchi, Y.; Izawa, H.; Miura, O.; Demura, S.; et al. Pressure-Induced Enhancement of Superconductivity in BiS2-Layered LaO1-xFxBiS2. *J. Phys. Soc. Jpn.* **2014**, *83*, 063704.
- (41) Nakashima, S.; Hangyo, M. Characterization of Low Dimensional Materials by Raman Spectroscopy. *Croat. Chem. Acta* **1988**, *61*, 331–346.
- (42) Scelta, D.; Baldassarre, A.; Serrano-Ruiz, M.; Dziubek, K.; Cairns, A. B.; Peruzzini, M.; Bini, R.; Ceppatelli, M. Interlayer Bond Formation in Black Phosphorus at High Pressure. *Angew. Chem.* **2017**, *129*, 14323–14328.
- (43) Jamieson, J. C. Crystal Structures Adopted by Black Phosphorus at High Pressures. *Science* **1963**, *139*, 1291–1292.
- (44) Chi, Z.-H.; Zhao, X.-M.; Zhang, H.; Goncharov, A. F.; Lobanov, S. S.; Kagayama, T.; Sakata, M.; Chen, X.-J. Pressure-Induced Metallization of Molybdenum Disulfide. *Phys. Rev. Lett.* **2014**, *113*, 036802.
- (45) Nayak, A. P.; Bhattacharyya, S.; Zhu, J.; Liu, J.; Wu, X.; Pandey, T.; Jin, C.; Singh, A. K.; Akinwande, D.; Lin, J.-F. Pressure-Induced Semiconducting to Metallic Transition in Multilayered Molybdenum Disulphide. *Nat. Commun.* **2014**, *5*, 3731.

- (46) Evarestov, R. A.; Kuzmin, A. Origin of Pressure-Induced Insulator-to-Metal Transition in the van Der Waals Compound FePS3 from First-Principles Calculations. *J. Comput. Chem.* **2020**, *41*, 1337–1344.
- (47) Zheng, Y.; Jiang, X.; Xue, X.; Dai, J.; Feng, Y. *Ab Initio* Study of Pressure-Driven Phase Transition in FePS3 and FePSe3. *Phys. Rev. B* **2019**, *100*, 174102.
- (48) Zhao, Z.; Zhang, H.; Yuan, H.; Wang, S.; Lin, Y.; Zeng, Q.; Xu, G.; Liu, Z.; Solanki, G. K.; Patel, K. D.; et al. Pressure Induced Metallization with Absence of Structural Transition in Layered Molybdenum Diselenide. *Nat. Commun.* **2015**, *6*, 7312.
- (49) Rifliková, M.; Martoňák, R.; Tosatti, E. Pressure-Induced Gap Closing and Metallization of MoSe2 and MoTe2. *Phys. Rev. B* **2014**, *90*, 035108.
- (50) Bera, A.; Singh, A.; Sorb, Y. A.; Jenjeti, R. N.; Muthu, D. V. S.; Sampath, S.; Narayana, C.; Waghmare, U. V.; Sood, A. K. Chemical Ordering and Pressure-Induced Isostructural and Electronic Transitions in MoSSe Crystal. *Phys. Rev. B* **2020**, *102*, 014103.
- (51) Zhu, L.; Wang, H.; Wang, Y.; Lv, J.; Ma, Y.; Cui, Q.; Ma, Y.; Zou, G. Substitutional Alloy of Bi and Te at High Pressure. *Phys. Rev. Lett.* **2011**, *106*, 145501.
- (52) Yesudhas, S.; Natarajan, S.; Thoguluva, R. High Pressure Raman Spectroscopy of Layered Matlockite, PbFCl. *J. Phys. Condens. Matter Inst. Phys. J.* **2013**, *25*, 155401.
- (53) Heyd, J.; Scuseria, G. E.; Ernzerhof, M. Hybrid Functionals Based on a Screened Coulomb Potential. *J. Chem. Phys.* **2003**, *118*, 8207–8215.
- (54) Heyd, J.; Scuseria, G. E.; Ernzerhof, M. Erratum: "Hybrid Functionals Based on a Screened Coulomb Potential" [J. Chem. Phys. 118, 8207 (2003)]. *J. Chem. Phys.* **2006**, *124*, 219906.
- (55) Attanayake, N. H.; Thenuwara, A. C.; Patra, A.; Aulin, Y. V.; Tran, T. M.; Chakraborty, H.; Borguet, E.; Klein, M. L.; Perdew, J. P.; Strongin, D. R. Effect of Intercalated Metals on the Electrocatalytic Activity of 1T-MoS2 for the Hydrogen Evolution Reaction. *ACS Energy Lett.* **2017**, *3*, 7–13.

TOC Graphic

